Thermal Spin-Current Generation in the Multifunctional Ferrimagnet $Ga_{0.6}Fe_{1.4}O_3$

Alberto Anadón,[1,*] Elodie Martin,[1] Suvidyakumar Homkar,[2] Benjamin Meunier,[2] Maxime Vergés,[1] Heloise Damas,[1] Junior Alegre,[1] Christophe Lefevre,[2] Francois Roulland,[2] Carsten Dubs,[3] Morris Lindner,[3] Ludovic Pasquier,[1] Olivier Copie,[1] Karine Dumesnil,[1] Rafael Ramos,[4] Daniele Preziosi,[2] Sébastien Petit-Watelot,[1] Nathalie Viart,[2] and Juan-Carlos Rojas-Sánchez[1,†]

[1] *Institut Jean Lamour, Université de Lorraine CNRS UMR 7198, Nancy, France*

[2] *Université de Strasbourg, CNRS, IPCMS, UMR 7504, Strasbourg F-67000, France*

[3] *INNOVENT e.V. Technologieentwicklung, Jena, Germany*

[4] *Departamento de Química-Física, Centro de Investigación en Química Biolóxica e Materiais Moleculares (CIQUS), Universidade de Santiago de Compostela, 15782, Spain*

(Received 27 June 2022; revised 26 August 2022; accepted 14 October 2022; published 29 November 2022)

In recent years, multifunctional materials have attracted increasing interest for magnetic memories and energy-harvesting applications. Magnetic insulating materials are of special interest for this purpose, since they allow the design of more efficient devices due to the lower Joule heat losses. In this context, $Ga_{0.6}Fe_{1.4}O_3$ (GFO) is a good candidate for spintronics applications, since it can exhibit multiferroicity and presents a spin Hall magnetoresistance similar to the one observed in a yttrium-iron-garnet (YIG)/Pt bilayer. Here, we explore GFO utilizing thermospin measurements in an on-chip approach. By carefully considering the geometry of our thermospin devices we are able to quantify the spin Seebeck effect and the spin-current generation in a GFO/Pt bilayer, obtaining a value comparable to that of YIG/Pt. This further confirms the promises of an efficient spin-current generation with the possibility of an electric field manipulation of the magnetic properties of the system in an insulating ferrimagnetic material.

DOI: 10.1103/PhysRevApplied.18.054087

I. INTRODUCTION

The search for multifunctional materials is nowadays a hot topic in spintronics [1,2]. Currently, functional devices are typically made of a bilayer composed of a nonmagnetic material with large spin-orbit coupling (NM) and a ferromagnetic material (FM). These types of devices allow functionalities such as the manipulation of the FM magnetization by the spin Hall effect (SHE) [3–5] in the NM or energy harvesting by employing its inverse counterpart, the inverse spin Hall effect [6]. Insulating magnetic materials (FMI) are preferred for this purpose to pave the way towards low dissipation spintronics devices [3]. Additional functionalities like the possibility of the electric field control of the magnetic properties of such systems could be given to these heterostructures by the introduction of multifunctional magnetic materials, opening the possibility of designing more efficient and versatile devices [7,8].

In spin Seebeck experiments [9–12] a thermal gradient is typically applied in the out-of-plane direction of the magnetic thin film, generating a spin current flowing alongside this direction. In insulating ferromagnetic materials, this spin current is carried by spin collective excitations, also called magnons, and can be injected into an adjacent layer such as Pt in the case of this study, and is then converted into a charge current via the inverse spin Hall effect (ISHE) [13–15]. This conversion occurs through the spin-orbit interaction of conduction electrons, which can be strong in heavy metals like Pt [16] and is given by [17]

$$\mathbf{E}_{\mathrm{ISHE}} = \frac{2e}{\hbar}\rho\,\theta_{\mathrm{SH}}\mathbf{J}_s \times \sigma, \tag{1}$$

where $\mathbf{E}_{\mathrm{ISHE}}$ is the electric field produced by the ISHE, e and $\hbar$ are the electron charge and reduced Plank constant, ρ is the resistivity of the Pt layer, θ_{SH} is the spin Hall angle, $\mathbf{J}_s$ is the spin current injected into Pt and σ its spin polarization.

Until now, yttrium iron garnet (YIG) has been the cornerstone material in thermospin phenomena due to its insulating nature and its unique magnetic properties such as low damping and coercive field. Here, we study the thermospin current generation in bilayers composed of Pt and the multifunctional magnetoelectric oxide $Ga_{0.6}Fe_{1.4}O_3$

*alberto.anadon@univ-lorraine.fr

†juan-carlos.rojas-sanchez@univ-lorraine.fr

(GFO) [18–20]. Engineering of thermospin devices with properly chosen dimensions allowed an accurate determination of the thermospin voltages necessary to calculate the spin Seebeck coefficient, and therefore granting a comparison with other systems. Indeed, the spin Seebeck effect (SSE) as well as the spin Hall magnetoresistance [21–23] in the GFO system are largely comparable with YIG-based ones. Furthermore, to corroborate our experimental finding we resort to finite-element simulations of the thermal profile to obtain an accurate heat flux in both GFO and YIG layers.

II. METHODS

A. Growth and structural characterization

GFO films are prepared by pulsed-laser deposition (PLD) on $SrTiO_3(111)$ substrates (Furuuchi Chemical Corporation, Japan, with root-mean-square roughness lower than 0.15 nm) maintained at 900 °C. The KrF excimer laser ($\lambda = 248$ nm) is operated with a fluence of 4 J/cm^2 [23] and a repetition rate of 2 Hz. The growth is done from a stoichiometric GFO target in an atmosphere of 0.1 mBar of O_2. The YIG film is grown by liquid phase epitaxy on 3-in. (111)-oriented gadolinium gallium garnet (GGG) substrate from PbO-B_2O_3-based high-temperature solution (HTL) at about 800 °C using a standard dipping technique [24,25]. During the deposition time of 90 s, the substrate is rotated in the solution at 33 rpm and then pulled out. Subsequently, the solution residues are spun off from the sample surface above the HTL and the sample is pulled out of the hot heating zone. Platinum layers for the GFO-based samples are deposited by PLD *in situ* in order to avoid any surface contamination. The deposition is carried out at room temperature in order to avoid any metal-oxide interdiffusion, under vacuum (base pressure of 2×10^{-8} mbar) and with a deposition rate of 0.06 nm/s, as in Ref. [23].

Structural characterization of the samples is done by x-ray diffraction $\theta - 2\theta$ scans using a Rigaku Smart Lab diffractometer equipped with a rotating anode (9 kW) and monochromated copper radiation (1.54056 Å). The $\theta - 2\theta$ scan shown in Fig. 1 indicates that the system grows following the ($SrTiO_3$) STO(111)//GFO(001)/Pt(111) structure, i.e., with the GFO film oriented along the [001] direction. The presence of Laue oscillations for the Pt (111) reflection is an indication of a smooth Pt/GFO interface.

The thermospin devices Are made using conventional UV lithography. We choose the following stacking to perform our main experiments: STO//GFO(64 nm)/Pt(5 nm) and GGG//YIG(140 nm)/Pt(5 nm). The Pt thin film is first patterned by ion milling. The width and the length of the Pt bar are 10 and 270 μm, respectively. Then, an insulating SiO_2 layer with a thickness of 75 nm is grown by rf sputtering using a Si target and Ar^+ and O^{2-} plasma. In a third and last step the Au heater [Ti(10 nm)/Au(150 nm)] is evaporated using a conventional evaporator. Both the heater and the sample are patterned with four pads to measure their resistance using four probes for more precise estimation. The dimensions of the active part of the heater and the sample are 330×10 μm^2 and 270×10 μm^2, respectively. The current flows only in the direction of the heater on top of the sample and the nonstraight area of the heater is orders of magnitude farther away from the sample (μm versus nm) than the heater area on top of the sample and thus we would not expect any significant parasitic effects from it.

B. Thermospin measurements and estimation of heat-transport parameters

Thermospin measurements are carried out in these devices using an electromagnet to apply an external in-plane magnetic field (H) as shown in Fig. 2(a). A dc

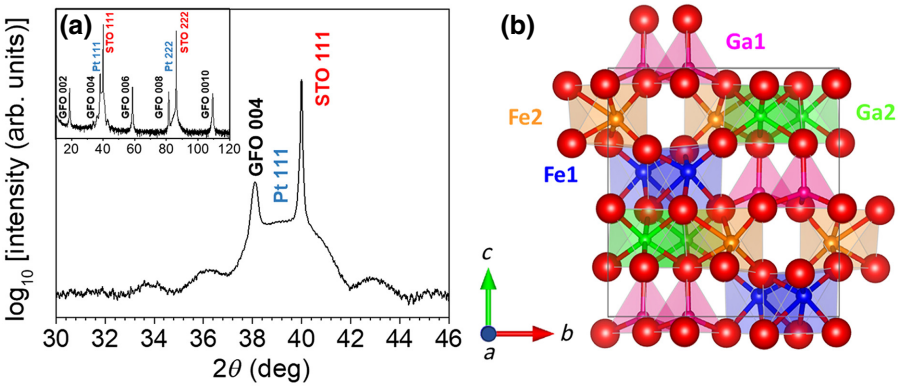

FIG. 1. Structural characterization. (a) X-ray diffraction $\theta - 2\theta$ scan showing the $Ga_{0.6}Fe_{1.4}O_3$ (004) peak, the Pt (111) peak and the associated Laue oscillations, indicating high crystalline coherence in the film and (b) crystal structure of $Ga_{0.6}Fe_{1.4}O_3$. In the crystallographic structure of GFO there are four different cationic sites that can be occupied by the Ga^{3+} and Fe^{3+} cations, named Ga1, Fe1, Ga2, and Fe2. Ga1 is a tetrahedral site, and the Fe1, Ga2, and Fe2 are nonequivalent octahedral sites.

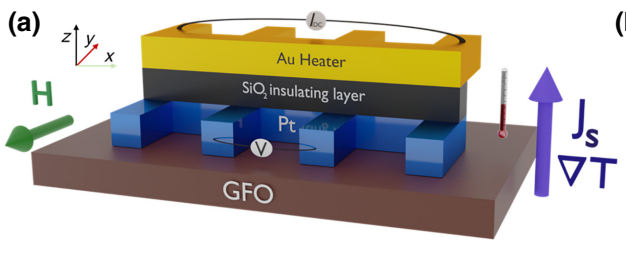

FIG. 2. Thermospin measurements. (a) Longitudinal spin Seebeck effect configuration. (b) Transversal voltage as a function of the in-plane field in a thermospin measurement with a heater current of 100 mA and (inset) picture of one of the thermospin devices.

current is passed through the heater and after 5 min of stabilization, the resistances of the sample and the heater are monitored using I-V measurements to avoid spurious contributions from thermal voltages. The thermospin voltage is monitored using a Keithley 2182a nano voltmeter.

Numerical simulations based on the finite-element method are performed by COMSOL Multiphysics, coupling the electric currents and heat-transfer modules, in order to quantify thermal gradients in GFO on STO substrate and in YIG on GGG substrate (see Appendix A). The cross-plane thermal conductivity of the GFO thin film is measured using the 3ω method. In this method a thin metal resistor simultaneously serves as a heater and a thermometer, it has been previously employed to determine the thermal conductivity of bulk and thin-film materials, details of the measurements can be found elsewhere [26–28]. For these measurements a Pt resistor (100 nm thick, 10 um width, 1 mm length with 10 nm of Cr for adhesion) is deposited on the bare GFO/STO heterostructure and the 3ω voltage response to an ac current with frequency is measured. The thermal parameters of the other layers are obtained from the literature [29–35] and detailed in Appendix A.

III. RESULTS

A. Thermospin voltage in GFO/Pt and YIG/Pt

We perform thermospin measurements in a GFO/Pt and YIG/Pt systems by observing the thermally induced voltage upon sweeping H as shown in Fig. 2(a) for GFO, obtaining a typical hysteresis looplike curve that follows the magnetization of the GFO thin film [23] [Fig. 2(b)] for a heater current of 100 mA. We perform these measurements for H applied at different directions in YIG and GFO and observed an isotropic behavior of the SSE voltage. In the case of YIG, the coercive field and saturation fields are much smaller than in GFO. It is worthwhile to note that, since GFO is an insulating material and we previously observe that the proximity in GFO/Pt is almost negligible at room temperature [23], we consider that this thermospin voltage comes fully from the SSE and there is not a significant anomalous Nernst effect contribution from the proximity in Pt.

By monitoring the magnitude of the thermospin voltage at saturation for different heater powers we can observe that the voltage difference between the saturation at positive and negative fields scales linearly with the power applied to the heater, as expected by the origin of the spin current generated in GFO. This is shown in the insets of Fig. 3 for both GFO and YIG systems. We also observe here that the order of magnitude of the SSE voltage is similar in both systems, although in the GFO, the offset voltage of the loop and the coercive field are significantly larger than in YIG. While the elucidation of the origin of such offset voltage is out of the scope of this paper, we argue that it might be related to a parasitic thermoelectric effect.

B. Quantitative comparison of the spin Seebeck effect in YIG and GFO

The determination of the spin Seebeck coefficient is normally subjected to large uncertainty due to the low reproducibility of the experimental conditions. Typically, in the literature, the SSE coefficient is defined as the ratio between the SSE voltage and the thermal gradient in the FM thin film normalized by the sample resistance [36].

$$S_{\mathrm{SSE}}^{\nabla T} = \frac{V^{\mathrm{ISHE}}}{\nabla T R_{\mathrm{Pt}} l}, \tag{2}$$

where V^{ISHE} is the thermospin voltage difference between positive and negative saturation fields divided by 2, ∇T is the thermal gradient through the FMI, R_{Pt} is the four-probe resistance in the Pt using I-V measurements and l is the distance between the voltage contacts.

Two steps can be taken to overcome the issue of low reproducibility in SSE measurements: first, the heat flux in the system can be considered instead of an estimation of the thermal gradient [37], and second, it is possible to maximize the reproducibility of the thermal conditions by using on-chip devices for a consistent thermal contact and dimensions of the system [38–40].

Following both of these steps, we propose to define the SSE coefficient considering the heat flux instead of the thermal gradient in the FMI (S_{SSE}^{q}) as follows:

$$S_{\mathrm{SSE}}^{\phi_q} = \frac{V^{\mathrm{ISHE}}}{\phi_q R_{\mathrm{Pt}}}, \tag{3}$$

where ϕ_q is the heat flux through the FMI.

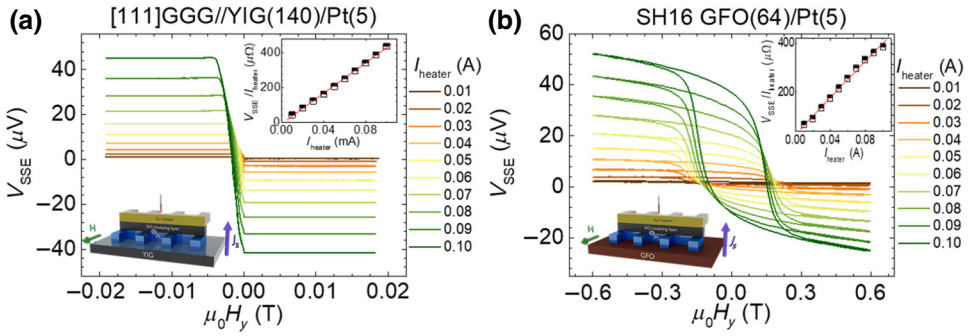

FIG. 3. Spin Seebeck effect in GFO and YIG. A comparable spin Seebeck voltage is obtained in the GFO/Pt and in the YIG/Pt system varying the heater power. The insets show the linear behavior of the thermospin voltage with the heater power.

To reliably compare the thermospin voltage in the GFO/Pt and YIG/Pt systems we compute the $S_{SSE}^{\phi_q}$ from Eq. (3) and obtain a comparable value for both systems as depicted in Table I. We obtain a $S_{SSE}^{\phi_q} = 2.9 \pm 0.3$ fV m^2/WΩ for GFO, whereas for YIG the value is slightly larger, 3.6 ± 0.4. This suggests that the efficiency of the spin-current generation in GFO is similar to that of YIG, opening possibilities in spin caloritronics using insulating magnetic materials with predicted tunable magnetic properties by electric fields.

Using the thermal conductivity for both FMI we can also estimate the thermal gradient in the FMI layers considering Fourier's law and a one-dimensional thermal flux ($\phi_{\mathbf{q}} = -\kappa \nabla T$) to compare with other studies in the literature as shown in Table I. We observe that the temperature difference between the upper and lower boundaries of the FMI in both systems are similar in magnitude under these considerations. To assess possible deviations from this simplified model due to the geometry of the device and possible thermal losses, we perform a finite-element simulation using COMSOL. In this simulation, we introduce the geometry of the system and use a combination of the electric currents and heat-transfer modules and we obtain a temperature difference in the FMI layer slightly smaller but comparable to the one calculated by Fourier's law for both systems. Figures 4(a) and 4(b) show, respectively, the local temperature distribution in the device in both $X0Z$ and $0YZ$ cut planes. They show that the temperature gradient direction is mostly out of plane within the device, as expected. The heat flux through the GFO layer is almost constant as shown in Fig. 4(c), indicating that the thermal losses are not relevant and the direction of the thermal gradient is almost completely out of plane in the GFO. Figure 4(d) shows the simulated thermal profile in the whole device.

In the case of GFO, we estimate the thermal conductivity using the 3ω method to be $\kappa_{GFO} = 4 \pm 1$ W/mK, significantly smaller than that of YIG [29]. The rest of the values considered are extracted from the literature [29–35]. Following these estimations, the value of the SSE considering the thermal gradient in the FMI can be recovered to compare with other studies. The calculated values of $S_{SSE}^{\nabla T}$ are 90 ± 10 and 160 ± 20 pV/KΩ respectively. The rest of the parameters to obtain them are shown in Table I. It is useful to consider that the GFO sample is not yet completely saturated at 0.6 T. We estimate using vibrating magnetometry measurements in a similar sample that we are underestimating the saturation thermospin voltage by 20%. We obtain a value of $S_{SSE}^{\nabla T}$ within the same order of magnitude and a similar value of $S_{SSE}^{\phi_q}$ for both materials, showing that for both methods of estimating the spin-current generation point towards the interest in using GFO as a promising functional material in insulating spintronics, e.g., for self-sustaining voltage-sensing applications. A change in the magnetic properties by an electric field can be monitored through a thermal gradient without supplying any electrical power, but waste heat. In short, a thermal gradient would generate the SSE voltage and this voltage will depend on the electric field that the device is subjected to. Another example would be the control of the coercive field by an electric field for efficient sensing of the magnetic field around a determined value similarly to how the operating point works in transistors. In addition,

TABLE I. Thermospin and thermal transport parameters for YIG and GFO at room temperature. Electrical resistivity, heat flux spin Seebeck coefficient, thermal conductivity of the FMI, estimated temperature difference between the upper and lower boundaries of the FMI layer for a heater current of 100 mA using Fourier's law and COMSOL simulations and thermal gradient spin Seebeck coefficient (traditional estimation method). The thickness of the FMI are 64 and 140 nm for the GFO and YIG films, respectively. We do not consider the interfacial thermal resistance in the estimation of the thermal gradients in the system.

	ρ_{Pt} ($\mu\Omega$ cm)	$S_{SSE}^{\phi_q}$ (fV m^2/WΩ)	κ_{FMI} (W/m K)	$\nabla T_{FMI}^{Fourier}$ (K)	∇T_{FMI}^{COMSOL} (K)	$S_{SSE}^{\nabla T}$ (pV/KΩ)
GFO/Pt	27.5	**2.9 ± 0.3**	4 ± 1	0.251	0.191	90 ± 10
YIG/Pt	25.3	**3.6 ± 0.4**	8.5	0.252	0.190	160 ± 20

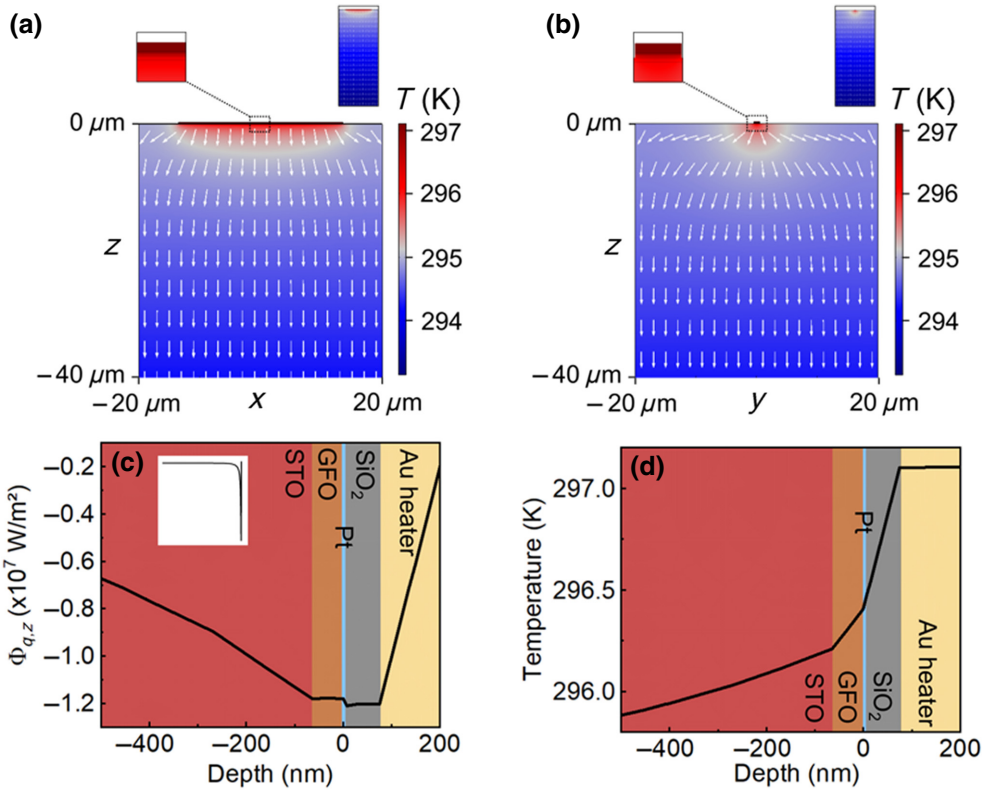

FIG. 4. Thermal simulation profile for the STO//GFO/Pt thermospin device. Calculated local temperature within the device that results from heating: (a) ($X0Z$) cut plane and (b) ($0YZ$) cut plane. The insets show the same distribution near the device (top left) and at an expanded range through the whole system (top right). (c) z component of heat flux in the out-of-plane direction at the center of the device as calculated by the numerical method. The inset extends the range in depth including the substrate, showing that the heat flux close to the bottom of the substrate vanishes. (d) Temperature in the out-of-plane direction at the center of the device as calculated by the numerical method.

it could potentially help feeding low-power devices in a similar fashion to other thermoelectric generators. These applications are especially interesting for the Internet of Things or wearable devices, where a battery is difficult to implement or is not desired.

IV. CONCLUSIONS

In summary, we explore the thermospin properties of the multifunctional material $Ga_{0.6}Fe_{1.4}O_3$ in the form of thin film for energy harvesting and thermal management applications. This material provides additional functionality in terms of ferroelectricity while maintaining the electrically insulating behavior compared to other materials such as yttrium iron garnet. By using an on-chip approach to increase reproducibility and carefully considering the heat flux and thermal gradients in both systems, we find that the spin-current generation by thermal excitation is comparable to the one of yttrium iron garnet. This observation supports the promises of an efficient spin-current generation with the possibility of an electric field manipulation of the magnetic properties of the system in an insulating ferrimagnetic material. Our results show that this material can be exploited in spintronics and spin caloritronics applications.

ACKNOWLEDGMENTS

This work is funded by the French National Research Agency (ANR) through the ANR-18-CE24-0008-01 "ANR MISSION" and the No. ANR-19-CE24-0016-01 "Toptronic ANR". S.H. acknowledges the Interdisciplinary Thematic Institute QMat, as part of the ITI 2021 2028 program of the University of Strasbourg, CNRS and Inserm, supported by IdEx Unistra (ANR 10 IDEX 0002), SFRI STRAT'US project (ANR 20 SFRI 0012), ANR-11-LABX-0058 NIE, and ANR-17-EURE-0024 under the framework of the French Investments for the Future Program. M.L. acknowledges the funding by the German Bundesministerium für Wirtschaft und Energie (BMWi)—49MF180119. R.R. also acknowledges support from the European Commission through the Project 734187-SPICOLOST (H2020-MSCA-RISE-2016), the European Union's Horizon 2020

research and innovation program through the MSCA Grant Agreement SPEC No. 894006, Grant RYC 2019-026915-I, Grant TED2021-130930B-I00 funded by the MCIN/AEI/10.13039/501100011033, by "ESF investing in your future" and by "NextGenerationEU"/PRTR, the Xunta de Galiciaa (ED431F 2022/04, ED431B 2021/013, Centro Singular de Investigación de Galicia Accreditation 2019-2022, ED431G 2019/03) and the European Union (European Regional Development Fund—ERDF). We also thank B. Wenzel, R. Meyer, M. Reich, and O. Surzhenko (INNOVENT) for their support.

APPENDIX A: SIMULATION OF THE THERMAL PROFILES IN GFO/Pt and YIG/Pt

1. Parameters for the finite-element simulation of the thermal profile in GFO/Pt and YIG/Pt

Thermal gradients are calculated in GFO on STO substrate and in YIG on GGG substrate by finite-element method (FEM) simulations in COMSOL Multiphysics software by coupling electric currents and heat-transfer modules. An electric current density $j_c = 6 \times 10$ A/m^2 flows into the Au wire while temperature is fixed at 293.15 K on the bottom of the substrate. We use thermal insulation condition on all the external boundaries (except the one whose temperature is fixed at room temperature) and thin layer condition for the Pt layer. We consider a Pt(5 nm)/SiO_2(75 nm)/Au(150 nm) wire (27 × 1 um) on either GGG (100 μm)/YIG (140 nm) or STO (100 μm)/GFO (64 nm). All the parameters of interest for each material are indicated in Table II.

TABLE II. Parameters for the thermal simulations using COMSOL. *Specific heat capacity (C_p) of GFO is not available in the literature, so the C_p of SiO_2 is used.

	t (nm)	κ (W/m K)	C_p (J/Kg K)	ρ (Kg/m^3)
GFO	64	4 ± 1 (this paper)	680*	5530
YIG	140	8.5 [29]	600 [30]	5170
STO	100 000	12 [31,32]	437 [32,33]	4891
GGG	100 000	7.5 [34]	380 [35]	7080
SiO_2	75	1.3	680	2 270
Pt	5	69.1	130	21 450
Au	150	310	130	19 300
Air	225	0.0262	1 003	1.225

2. Finite-element simulation of the thermal profile in YIG

A finite-element simulation is also carried out using the parameters of the YIG/Pt sample as shown in Table II. The resulting thermal and heat-flux profiles are similar to the ones in GFO and can be observed in Fig. 5.

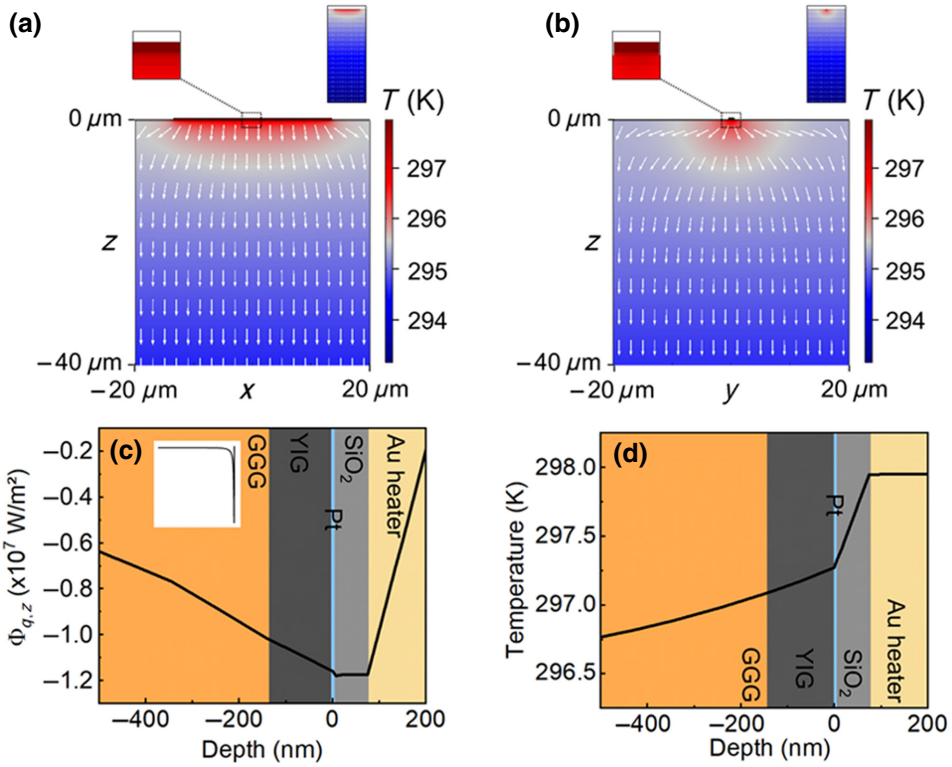

FIG. 5. Thermal simulation profile for the GGG//YIG/Pt thermospin device. Calculated local temperature within the device that results from heating with (a) ($X0Z$) cut plane and (b) ($0YZ$) cut plane. The insets show the same distribution near the device (top left) and at an expanded range through the whole system (top right). (c) z component of heat flux in the out-of-plane direction at the center of the device as calculated by the numerical method. The inset presents the same information in the stack including the substrate. (d) Temperature in the out-of-plane direction at the center of the device as calculated by the numerical method.

[1] Wilma Eerenstein, N. D. Mathur, and James F. Scott, Multiferroic and magnetoelectric materials, Nature **442**, 759 (2006).

[2] J. F. Scott, Multiferroic memories, Nat. Mater. **6**, 256 (2007).

[3] Can Onur Avci, Andy Quindeau, Chi-Feng Pai, Maxwell Mann, Lucas Caretta, Astera S. Tang, Mehmet C. Onbasli, Caroline A. Ross, and Geoffrey S. D. Beach, Current-induced switching in a magnetic insulator, Nat. Mater. **16**, 309 (2017).

[4] Kevin Garello, Can Onur Avci, Ioan Mihai Miron, Manuel Baumgartner, Abhijit Ghosh, Stéphane Auffret, Olivier Boulle, Gilles Gaudin, and Pietro Gambardella, Ultrafast magnetization switching by spin-orbit torques, Appl. Phys. Lett. **105**, 212402 (2014).

[5] Alberto Anadon, Ruben Guerrero, Jorge Alberto Jover-Galtier, Adrian Gudin, Jose Manuel Diez Toledano, Pablo Olleros-Rodriguez, Rodolfo Miranda, Julio Camarero, and Paolo Perna, Spin-orbit torque from the introduction of Cu interlayers in Pt/Cu/Co/Pt nanolayered structures for spintronic devices, ACS Appl. Nano Mater. **4**, 487 (2020).

[6] R. Ramos, A. Anadón, I. Lucas, K. Uchida, P. A. Algarabel, L. Morellón, M. H. Aguirre, E. Saitoh, and M. R. Ibarra, Thermoelectric performance of spin Seebeck effect in Fe_3O_4/pt-based thin film heterostructures, APL Mater. **4**, 104802 (2016).

[7] Sasikanth Manipatruni, Dmitri E. Nikonov, Chia-Ching Lin, Tanay A. Gosavi, Huichu Liu, Bhagwati Prasad, Yen-Lin Huang, Everton Bonturim, Ramamoorthy Ramesh, and Ian A. Young, Scalable energy-efficient magnetoelectric spin-orbit logic, Nature **565**, 35 (2019).

[8] Ramamoorthy Ramesh, Emerging routes to multiferroics, Nature **461**, 1218 (2009).

[9] K. Uchida, M. Ishida, T. Kikkawa, A. Kirihara, T. Murakami, and E. Saitoh, Longitudinal spin Seebeck effect: From fundamentals to applications, J. Phys.: Condens. Matter **26**, 343202 (2014).

[10] Alberto Anadón, Adrián Gudín, Rubén Guerrero, Iciar Arnay, Alejandra Guedeja-Marron, Pilar Jiménez-Cavero, Jose Manuel Díez Toledano, Fernando Ajejas, María Varela, Sebastien Petit-Watelot, *et al.*, Engineering the spin conversion in graphene monolayer epitaxial structures, APL Mater. **9**, 061113 (2021).

[11] Ken-ichi Uchida, J. Xiao, Hiroto Adachi, Jun-ichiro Ohe, S. Takahashi, J. Ieda, T. Ota, Y. Kajiwara, H. Umezawa, H. Kawai, *et al.*, Spin Seebeck insulator, Nat. Mater. **9**, 894 (2010).

[12] Ken ichi Uchida, Hiroto Adachi, Takashi Kikkawa, Akihiro Kirihara, Masahiko Ishida, Shinichi Yorozu, Sadamichi Maekawa, and Eiji Saitoh, Thermoelectric generation based on spin Seebeck effects, Proc. IEEE **104**, 1946 (2016).

[13] Axel Hoffmann, Spin Hall effects in metals, IEEE Trans. Magn. **49**, 5172 (2013).

[14] Jairo Sinova, Sergio O. Valenzuela, Jörg Wunderlich, C. H. Back, and T. Jungwirth, Spin Hall effects, Rev. Mod. Phys. **87**, 1213 (2015).

[15] S. M. Rezende, R. L. Rodríguez-Suárez, R. O. Cunha, A. R. Rodrigues, F. L. A. Machado, G. A. Fonseca Guerra, J. C. Lopez Ortiz, and A. Azevedo, Magnon spin-current theory for the longitudinal spin-Seebeck effect, Phys. Rev. B **89**, 014416 (2014).

[16] C. Guillemard, S. Petit-Watelot, S. Andrieu, and J.-C. Rojas-Sánchez, Charge-spin current conversion in high quality epitaxial Fe/Pt systems: Isotropic spin Hall angle along different in-plane crystalline directions, Appl. Phys. Lett. **113**, 262404 (2018).

[17] T. Kikkawa, D. Reitz, H. Ito, T. Makiuchi, T. Sugimoto, K. Tsunekawa, S. Daimon, K. Oyanagi, R. Ramos, S. Takahashi, Y. Shiomi, Y. Tserkovnyak, and E. Saitoh, Observation of nuclear-spin Seebeck effect, Nat. Commun. **12**, 4356 (2021).

[18] Amritendu Roy, Somdutta Mukherjee, Rajeev Gupta, Rajendra Prasad, and Ashish Garg, Structure and properties of magnetoelectric gallium ferrite: A brief review, Ferroelectrics **473**, 154 (2014).

[19] Daniel Stoeffler, First principles study of the electric polarization and of its switching in the multiferroic $GaFeO_3$ system, J. Phys.: Condens. Matter **24**, 185502 (2012).

[20] Tsukasa Katayama, Shintaro Yasui, Yosuke Hamasaki, Takahisa Shiraishi, Akihiro Akama, Takenori Kiguchi, and Mitsuru Itoh, Ferroelectric and magnetic properties in room-temperature multiferroic $Ga_xFe_{2-x}O_3$ epitaxial thin films, Adv. Funct. Mater. **28**, 1704789 (2018).

[21] Matthias Althammer, *et al.*, Quantitative study of the spin Hall magnetoresistance in ferromagnetic insulator/normal metal hybrids, Phys. Rev. B **87**, 224401 (2013).

[22] H. Nakayama, M. Althammer, Y.-T. Chen, K. Uchida, Y. Kajiwara, D. Kikuchi, T. Ohtani, S. Geprägs, M. Opel, S. Takahashi, R. Gross, G. E. W. Bauer, S. T. B. Goennenwein, and E. Saitoh, Spin Hall Magnetoresistance Induced by a Nonequilibrium Proximity Effect, Phys. Rev. Lett. **110**, 206601 (2013).

[23] Suvidyakumar Homkar, Elodie Martin, Benjamin Meunier, Alberto Anadon-Barcelona, Corinne Bouillet, Jon Gorchon, Karine Dumesnil, Christophe Lefèvre, François Roulland, Olivier Copie, *et al.*, Spin current transport in hybrid Pt/multifunctional magnetoelectric $Ga_{0.6}Fe_{1.4}O_3$ bilayers, ACS Appl. Electron. Mater. **3**, 4433 (2021).

[24] E. A. Giess, in *Vapour Growth and Epitaxy* (Elsevier, 1975), p. 358.

[25] Carsten Dubs, Oleksii Surzhenko, Ralf Linke, Andreas Danilewsky, Uwe Brückner, and Jan Dellith, Sub-micrometer yttrium iron garnet LPE films with low ferromagnetic resonance losses, J. Phys. D: Appl. Phys. **50**, 204005 (2017).

[26] David G. Cahill, Thermal conductivity measurement from 30 to 750 K: The 3ω method, Rev. Sci. Instrum. **61**, 802 (1990).

[27] E. Langenberg, E. Ferreiro-Vila, V. Leborán, A. O. Fumega, V. Pardo, and F. Rivadulla, Analysis of the temperature dependence of the thermal conductivity of insulating single crystal oxides, APL Mater. **4**, 104815 (2016).

[28] P. Jiménez-Cavero, I. Lucas, D. Bugallo, C. López-Bueno, R. Ramos, P. A. Algarabel, M. R. Ibarra, F. Rivadulla, and L. Morellón, Quantification of the interfacial and bulk contributions to the longitudinal spin Seebeck effect, Appl. Phys. Lett. **118**, 092404 (2021).

[29] C. Euler, P. Hołuj, T. Langner, A. Kehlberger, V. I. Vasyuchka, M. Kläui, and G. Jakob, Thermal conductance

of thin film YIG determined using Bayesian statistics, Phys. Rev. B **92**, 094406 (2015).

[30] Stephen R. Boona and Joseph P. Heremans, Magnon thermal mean free path in yttrium iron garnet, Phys. Rev. B **90**, 064421 (2014).

[31] Yasutaka Suemune, Thermal conductivity of $BaTiO_3$ and $SrTiO_3$ from 4.5 to 300 K, J. Phys. Soc. Jpn. **20**, 174 (1965).

[32] Annette Bussmann-Holder, A simple recipe to calculate the thermal conductivity of anharmonic crystals: The case of $SrTiO_3$, Ferroelectrics **553**, 26 (2019).

[33] Dominique de Ligny and Pascal Richet, High-temperature heat capacity and thermal expansion of $SrTiO_3$ and $SrZrO_3$ perovskites, Phys. Rev. B **53**, 3013 (1996).

[34] Baosong Wang, Haihe Jiang, Xiande Jia, Qingli Zhang, Dunlu Sun, and Shaotang Yin, Thermal conductivity of doped YAG and GGG laser crystal, Front. Optoelectron. China **1**, 138 (2008).

[35] D. A. Samoshkin and S. V. Stankus, Heat capacity of neodymium- and gadolinium-gallium garnets, J. Phys.: Conf. Ser. **1677**, 012175 (2020).

[36] Sergio M. Rezende, Antonio Azevedo, and Roberto L. Rodriguez-Suárez, Magnon diffusion theory for the spin Seebeck effect in ferromagnetic and antiferromagnetic insulators, J. Phys. D: Appl. Phys. **51**, 174004 (2018).

[37] A. Sola, P. Bougiatioti, M. Kuepferling, D. Meier, G. Reiss, M. Pasquale, T. Kuschel, and V. Basso, Longitudinal spin Seebeck coefficient: Heat flux vs. temperature difference method, Sci. Rep. **7**, 46752 (2017).

[38] Stephen M. Wu, Frank Y. Fradin, Jason Hoffman, Axel Hoffmann, and Anand Bhattacharya, Spin Seebeck devices using local on-chip heating, J. Appl. Phys. **117**, 17C509 (2015).

[39] Yongming Luo, Changjiang Liu, Hilal Saglam, Yi Li Wei Zhang, Steven S.-L. Zhang, John E. Pearson, Brandon Fisher, Tiejun Zhou, Anand Bhattacharya, and Axel Hoffmann, Distinguishing antiferromagnetic spin sublattices via the spin Seebeck effect, Phys. Rev. B **103**, L020401 (2021).

[40] Changjiang Liu, Yongming Luo, Deshun Hong, Steven S.-L. Zhang, Hilal Saglam, Yi Li Yulin Lin, Brandon Fisher, John E. Pearson, J. Samuel Jiang, Hua Zhou, Jianguo Wen, Axel Hoffmann, and Anand Bhattacharya, Electric field control of magnon spin currents in an antiferromagnetic insulator, Sci. Adv. **7**, eabg1669 (2021).